

Wind tunnel investigations on aerodynamics of a 2:1 rectangular section for various angles of wind incidence

M. Keerthana^{*1,2} and P. Harikrishna^{1,2a}

¹CSIR-Structural Engineering Research Centre, CSIR Madras Campus, Taramani, Chennai 600 113, India

²Academy of Scientific and Innovative Research, India

(Received February 27, 2017, Revised July 4, 2017, Accepted August 7, 2017)

Abstract. Multivariate fluctuating pressures acting on a 2:1 rectangular section (2-D) with dimensions of 9 cm by 4.5 cm has been studied using wind tunnel experiments under uniform and smooth flow condition for various angles of wind incidence. Based on the variation of mean pressure coefficient distributions along the circumference of the rectangular section with angle of wind incidence, and with the aid of skin friction coefficients, three distinct flow regimes with two transition regimes have been identified. Further, variations of mean drag and lift coefficients, Strouhal number with angles of wind incidence have been studied. The applicability of Universal Strouhal number based on vortex street similarity of wakes in bluff bodies to the 2:1 rectangular section has been studied for different angles of wind incidence. The spatio-temporal correlation features of the measured pressure data have been studied using Proper Orthogonal Decomposition (POD) technique. The contribution of individual POD modes to the aerodynamic force components, viz, drag and lift, have been studied. It has been demonstrated that individual POD modes can be associated to different physical phenomena, which contribute to the overall aerodynamic forces.

Keywords: rectangular section; drag; lift; pressure coefficient; skin friction coefficient; vortex shedding; universal Strouhal number; Proper Orthogonal Decomposition (POD); modes; eigen values

1. Introduction

Bluff body aerodynamics continues to be an area of active research from both basic and application standpoints. Rectangular sections are the most generic form of bluff bodies, which find common application in various engineering structures. Wind tunnel studies are considered the most reliable for understanding the complex aerodynamic characteristics of bluff bodies with respect to angle of wind incidence. In addition, the wind tunnel pressure measurements would also serve as benchmark for validating the results of the Computational Fluid Dynamics (CFD) simulations. One such benchmark study, Benchmark on the Aerodynamics of a Rectangular 5:1 Cylinder (BARC) has been carried out recently by International Association for Wind Engineering (IAWE) in order to provide a contribution to the analysis of the turbulent flow around a 5:1 rectangular cylinder using both experimental and numerical studies (Bartoli *et al.* 2009, Bruno *et al.* 2010, Mannini *et al.* 2017).

*Corresponding author, Ph.D. student, E-mail: keerthana@serc.res.in

^a Senior Principal Scientist, E-mail: hari@serc.res.in

It has led to a major Research and Development (R&D) thrust in the area of aerodynamic studies on rectangular sections. Rectangular sections with geometric proportion (the ratio of longer to shorter dimension, R) of 2:1 to 4:1 have been observed to be aerodynamically highly sensitive. This is due to the possibility of occurrence of intermittent reattachment of the separated shear layers along the longer dimension of the rectangular section for flow normal to the shorter dimension (Simiu and Scanlan 1996, Shimada and Ishihara 1999, Hemon and Santi 2002). Hence, aerodynamic characteristics of rectangular cylinders with value of R of 2:1, 3:1, 4:1 have been experimentally (Wang and Gu 2015, Matsumoto 1998; Amrouche *et al.* 2010, Noda and Nakayama 2003) as well as numerically (Yu and Kareem 1998, Shimada and Ishihara 2002) studied in detail. Angle of wind incidence and turbulence has been observed to significantly affect the flow characteristics of such bluff bodies (Dutta *et al.* 2003). However, most of the studies were carried out for flow normal to any one of the faces of the rectangular section. Further, it is of immense interest that rectangular sections with geometric proportion of 0.75 to 3 are also susceptible to galloping phenomenon (van Oudheusden *et al.* 2005, Keerthana and Harikrishna 2013). Recently, Gao and Zhu (2016) have carried out experimental investigations on galloping instability of 2:1 rectangular cylinder.

Further, most of the wind tunnel experiments that studied the effects of angles of wind incidence on 2:1 rectangular sections involved evaluation of aerodynamic force coefficients using force measurements (Matsumoto 1998) and/or evaluation of Strouhal number using vortex shedding frequency measurements (Knisely 1990, Okajima 1982, Hemon *et al.* 2001). Unsteady pressures on such rectangular sections with complex aerodynamic behavior is due to various wind induced physical phenomena acting simultaneously. Larose and D'Auteuil (2008) studied the aerodynamics of a 2:1 rectangular section using pressure measurements for limited angles of wind incidence of less than 10° . It has been observed that very few wind tunnel experimental studies on 2:1 rectangular sectional model involved pressure measurements for the evaluation of pressure coefficient distributions for various angles of wind incidence.

Hence, in the present study, wind tunnel pressure measurements have been carried out on a 2:1 rectangular section under 2-D, uniform and smooth flow condition with longitudinal turbulence intensity of about 0.5%, for various angles of wind incidence (α) between 0° (flow normal to shorter dimension) and 90° (flow normal to longer dimension). Based on the variation in distribution of mean pressure coefficient and skin friction coefficient with angle of wind incidence, five distinct flow regimes have been identified. Further, the variation of mean force coefficients, viz, mean drag and lift coefficients, and Strouhal number with angle of wind incidence have been discussed. The concept of Universal Strouhal number based on vortex street similarity of wakes in bluff bodies (Griffin 1981, Ahlborn *et al.* 2002) and its applicability for 2:1 rectangular section for the tested angles of wind incidence has been studied from a renewed perspective.

Further, spatio-temporal characteristics of the measured pressures have been studied using Proper Orthogonal Decomposition (POD) technique. POD is one of the widely adopted techniques to analyse multivariate data. It has been used for reduced order modeling (ROM), simulation of stochastic processes, probabilistic dynamics, etc. A more comprehensive review of the technique and its vast applications can be found in Solari *et al.* (2007) and Carassale *et al.* (2007). In the context of studies on bluff-body aerodynamics, where complex flow phenomena takes place, POD has been applied on square sections (de Grenet and Ricciardelli 2004), circular sections (Qiu *et al.* 2014, Zhang *et al.* 2014) and rectangular sections (Hoa *et al.* 2013). The coherent structures in the unsteady pressure field have been the focus of such studies. It has been observed that a few number of POD modes are sufficient to represent the results of wind tunnel experiments with good accuracy. Especially, the first POD mode has been observed to best represent the dominant flow phenomena

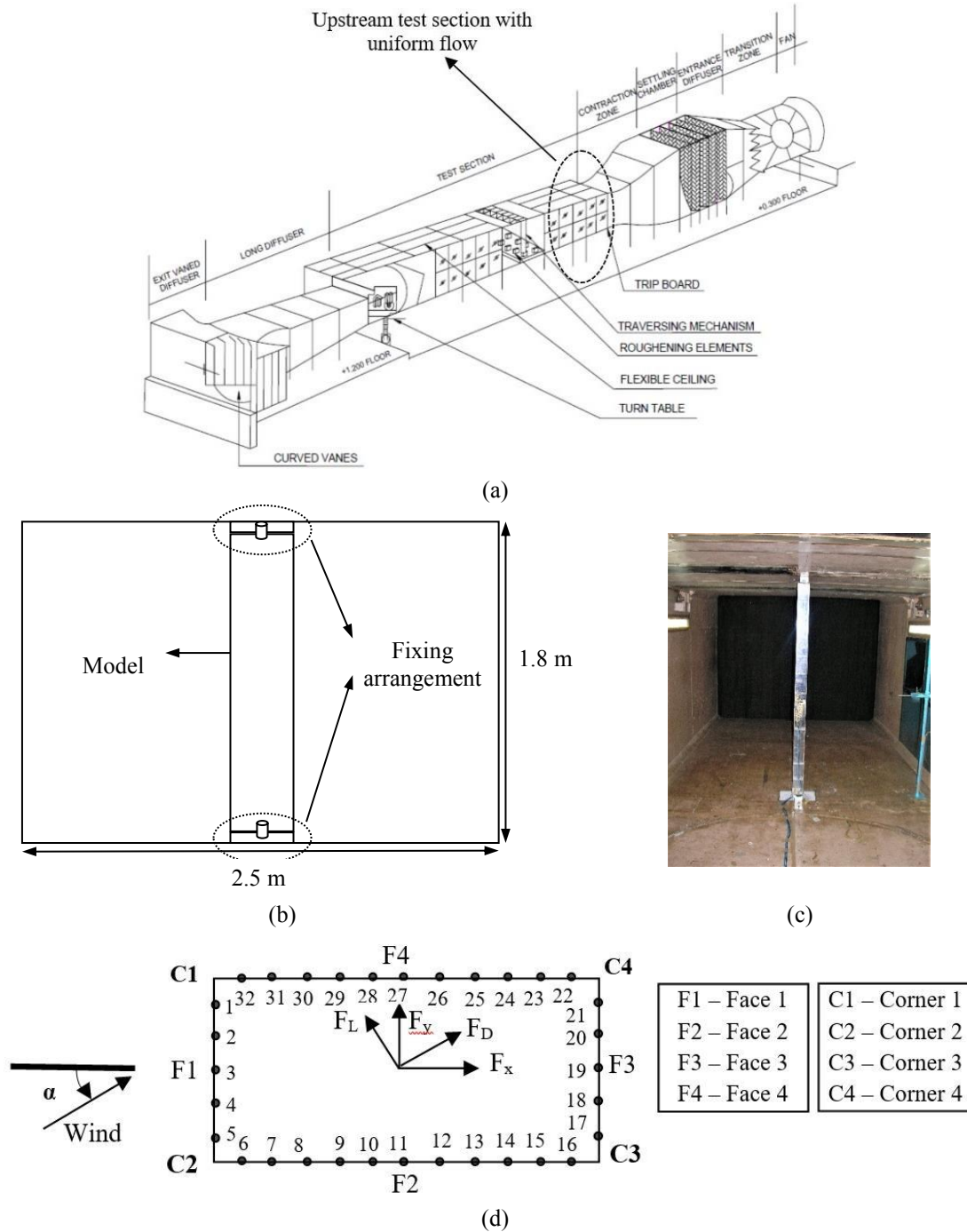


Fig. 1 (a) Boundary layer wind tunnel facility of CSIR-SERC, (b) Schematic view of the experimental setup, (c) Photograph of the model mounted in the upstream test section of wind tunnel and (d) Pressure tap lay out at the mid-height of the model

(Kikuchi *et al.* 1997, Carassale 2012). In the present study, the POD technique has been used to carry out spatio-temporal correlation studies of the fluctuating pressures on the 2:1 rectangular section for various angles of wind incidence to classify the flow regimes and to identify the POD modes contributing to the aerodynamic forces, viz. drag and lift.

2. Experimental investigations

The experiments involving pressure measurement have been carried out in the upstream test section of the Boundary Layer Wind Tunnel (BLWT) facility at CSIR-Structural Engineering Research Centre (CSIR-SERC) shown in Fig. 1(a). The flow at the upstream test section is uniform over the cross-section. The dimensions of the test section are 2.5 m (width) x 1.8 m (height). The length of the model has been chosen to be 1.8 m, so that it occupies full height of the wind tunnel section in vertical mounting position to achieve 2-D flow condition, with top and bottom walls of the wind tunnel acting as end plates. The cross-section dimensions of the sectional model of the rectangular section have been chosen to be 9 cm (B) x 4.5 cm (D), based on blockage ratio considerations. The maximum blockage ratio for the chosen dimension is 4% for angle of wind incidence (α) of 63.5° , for which the projected area of the rectangular section is maximum. The model has been fabricated using acrylic perspex material. It has been instrumented with 32 pressure taps along the periphery at mid-height (i.e., at 0.9 m) of the model (Fig. 1(d)), for simultaneous pressure measurements. Restrictor based pressure tubing system, with a length of 18 cm has been used in the present study. A 3 cm long metal restrictor with internal diameter of 0.3 mm connected two 8 cm long special PVC tubes with outer diameter of 1.6 mm and inner diameter of 0.8 mm. The metal restrictor has an overlap of 0.5 cm with the pressure tubes on either sides. The restrictor prevents attenuation of pressure fluctuations, and the tubing has flat frequency response characteristics up to 250 Hz. One end of this pressure tube has been attached to the model, while the other end has been connected to the pressure transducer. A pitot tube has been provided at the instrumented level of 0.9 m, to measure the velocity of the oncoming flow. Schematic view of the cross-section of the test section of the wind tunnel with rectangular sectional model is shown in Fig. 1(b). The sectional model of the 2:1 rectangular section mounted in the wind tunnel at the test section is shown in Fig. 1(c). Instantaneous pressures from the pressure taps were measured simultaneously using a Scanivalve pressure transducer at a sampling rate of 500 Hz for a sampling duration of 36 seconds. This duration corresponds to non-dimensional convective time unit (Ut/D) of 10080. BARC requirement of Reynolds number (Re) for benchmarking studies has been observed to be in the range of 0.2×10^5 to 0.6×10^5 , based on 'D' as characteristic dimension (Bruno *et al.* 2014). Hence, in line with the BARC guideline, the present study has been carried out at a Reynolds number of 0.6×10^5 , with a uniform wind velocity of 12.6 m/s and turbulence intensity of about 0.5%. The symmetry of the model has been confirmed by good agreement of the measured pressures for angle of wind incidence of 0° and 180° . Pressure measurements have been made under uniform and smooth flow for 29 angles of wind incidence, viz, $0^\circ, 2^\circ, 4^\circ, 6^\circ, 8^\circ, 10^\circ, 12^\circ, 14^\circ, 15^\circ, 20^\circ, 25^\circ, 30^\circ, 35^\circ, 40^\circ, 45^\circ, 50^\circ, 55^\circ, 60^\circ, 65^\circ, 67^\circ, 69^\circ, 71^\circ, 73^\circ, 75^\circ, 78^\circ, 81^\circ, 84^\circ, 87^\circ$ and 90° .

3. Statistical and spectral analysis of measured pressures

3.1 Probabilistic characteristics of the measured pressure data

Typical time history of measured pressures for pressure tap number 11 (central pressure tap) on face F2 (side face) for α of 0° has been shown in Fig. 2(a). The histogram of the probability density function of the standardised pressures (zero mean and unit normal) has been compared with Gaussian process in Fig. 2(b). Similarly, time history and histogram of the pressure from the pressure tap number 5 immediately after corner C2 on the face F1 for α of 90° have been shown in Figs. 3(a) and 3(b). It can be observed that the measured pressures at pressure taps located after flow separation are highly non-Gaussian in nature, with negative tailed probability distribution. Similar characteristics have been observed for all the pressure taps in the wake region, i.e., beyond the flow separation.

3.2 Evaluation of aerodynamic parameters

The measured pressures at every individual pressure tap have been multiplied with the corresponding tributary widths (Table 1) to evaluate the forces per unit length along the body fixed axes, viz, F_x and F_y as shown in Fig. 1(d). The drag (F_D) and lift (F_L) forces per unit length have been evaluated by suitably resolving F_x and F_y along and normal to the wind direction as given below.

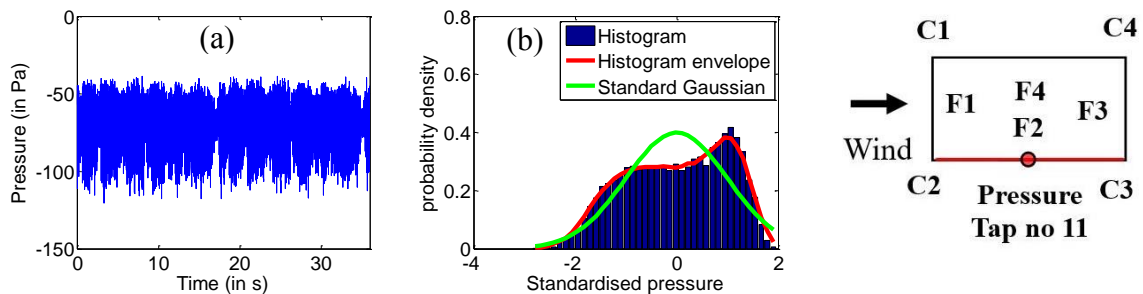


Fig. 2 (a) Time history of pressure and (b) Histogram of standardised pressure for central pressure tap in face F4 for 0°

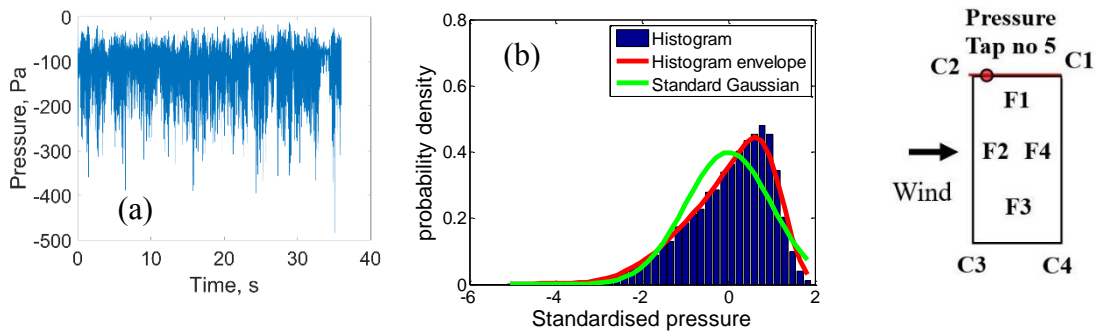


Fig. 3 (a) Time history of pressure and (b) Histogram of standardised pressure for pressure tap immediately after flow separation on the face F1 for 90°

Table 1 Tributary widths of pressure taps

S. No	Pressure tap numbers	Tributary widths (cm)
1	7,15,23,31	0.5
2	6,8,14,16,22,24,30,32	0.75
3	1,2,4,5,17,18,20,21	0.875
4	3,9,10,11,12,13,19,25,26,27,28,29	1

$$F_D = F_x \cos \alpha + F_y \sin \alpha; \quad F_L = -F_x \sin \alpha + F_y \cos \alpha \quad (1)$$

Further, the non-dimensional pressure coefficient (C_p), aerodynamic drag and lift coefficients (C_D^* and C_L^*) have been evaluated as

$$C_p = \frac{p}{\frac{1}{2} \rho U^2}; \quad C_D^* = \frac{F_D}{\frac{1}{2} \rho U^2 D^*}; \quad C_L^* = \frac{F_L}{\frac{1}{2} \rho U^2 D^*} \quad (2)$$

where U is the reference wind speed measured at the level of 0.9 m, ρ is the density of air, D^* is the characteristic reference dimension, which, for the present study is considered as the projected width of the rectangular section normal to the flow direction. Statistical and spectral analysis of the evaluated pressure coefficients and aerodynamic drag and lift coefficients have been carried out. Further, Strouhal number (St^*) has been evaluated as

$$St^* = \frac{f_s D^*}{U} \quad (3)$$

where, f_s is the vortex shedding frequency obtained from the peak of power spectral density function of pressures from pressure taps in the leeward portion of the rectangular section, where there is dominance of vortex shedding. The value of f_s obtained from individual pressure taps has been verified from the peak of power spectral density function of integrated lift forces. Typical mean pressure coefficient distribution for selected angles of wind incidence have been presented in Fig. 4.

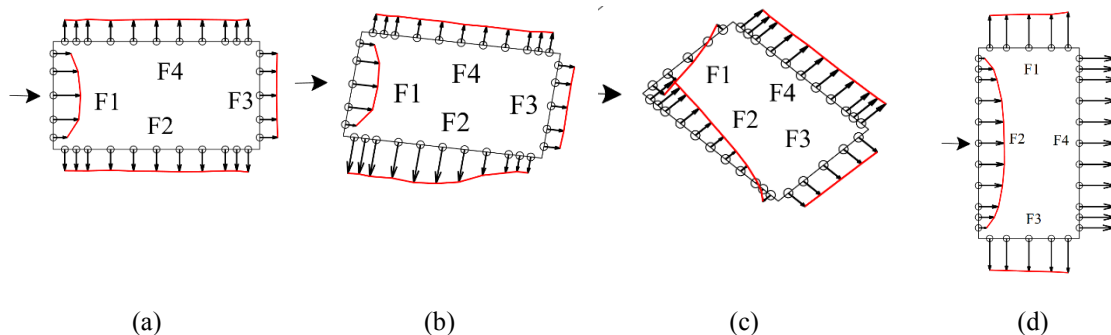


Fig. 4 Distribution of mean pressure coefficient for α of (a) 0° , (b) 8° , (c) 45° and (d) 90°

3.3 Mean pressure coefficients and Identification of flow regimes

The change in angle of wind incidence causes change in the location of separation points on the rectangular section and also change in the pattern of shear layers and formation of vortices, thereby creating distinct flow signatures. The occurrence of asymptotic minimum value of skin friction coefficient (C_f) coherent with the flattening of distribution of mean pressure coefficient has been reported by Cebeci *et al.* (1972) as indicators of boundary layer separation. Hence, skin friction coefficient (C_f), which is ratio of local shear stress on the surface of the rectangular section and dynamic pressure has been evaluated based on the empirical relationship given in Eq. (4). The relationship in Eq. (4) has been arrived based on numerous experimental investigations on the turbulent boundary layer characteristics of flat plates and bluff bodies (Schlichting 1979).

$$C_f = \frac{0.0592}{(Re_x)^{1/5}}; \text{ where } Re_x = \frac{U_x D}{\nu} \tag{4}$$

where Re_x is Reynolds number formed along the circumference of the bluff body, U_x is the velocity at the considered location (x) along the circumference of the bluff body, which has been evaluated from the experimentally obtained mean pressure coefficient (C_p) using Bernoulli's theorem. D is the shorter dimension of the rectangular section ($=0.045$ m) and ν is the kinematic viscosity of air. Based on the variation in distribution of mean pressure coefficient (C_p) and skin friction coefficient (C_f) with α , three distinct flow regimes have been identified along with two transition flow regimes for the flow around the 2:1 rectangular section as shown in Fig. 5.

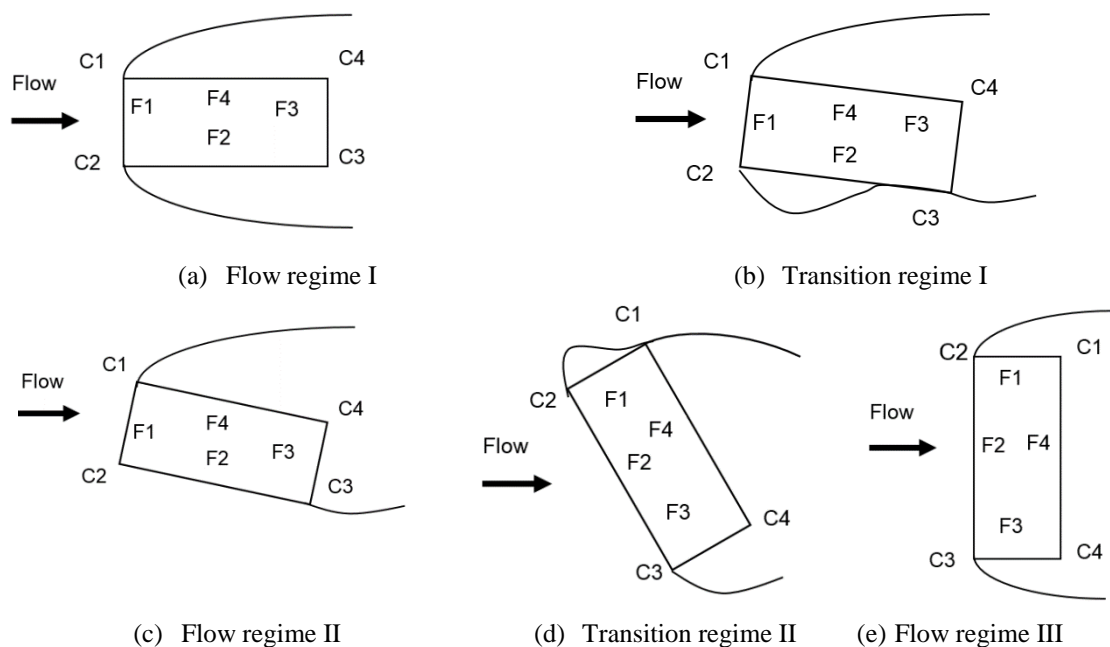


Fig. 5 Schematic representation of various assumed flow regimes around the rectangular section depending on α

Flow regime I involved separation of flow from the corners C1 and C2 (Fig. 5(a)). Figs. 6(a) and 6(b) shows the distribution of mean C_p and C_f for α of 0° and 2° in flow regime I. It has been observed that the value of C_f reduced to minimum value approximately at locations corresponding to the corners C1 and C2 of face F1, that is predominantly exposed to oncoming flow. Flatness in mean C_p distribution immediately after flow separation has also been observed (Cebeci *et al.* 1972).

Transition regime I (Fig. 5(b)) still involved separation of shear layers from corners C1 and C2, but the shear layer detaching from C2 has been observed to show tendency to reattach along the face F2, thereby forming a recirculation zone and further move downstream to separate at C3. This phenomenon in transition regime I is evident from the values of C_f on the surface of the 2:1 rectangular section. The C_f has been observed to reach a minimum value at corners C1 and C2 (Fig. 7(b) which covers typical α between 4° and 25°) and showed increasing trend along the face F2 and further reduced to minimum value at corner C3. The occurrence of the minimum value of C_f at corner C3 has been followed by nearly constant values of C_f , which is indicative of flow separation.

This movement of separation point from C2 to C3 causes reduction in wake width. It can be seen from the mean pressure distribution for the aforementioned transition regime I (Fig. 7(a)) that the mean C_p values in the base pressure region (face F3) is more or less same, but on the face F2, distinct trends of pressure recovery have been observed. The reduced wake width, as mentioned earlier facilitates better pressure recovery (Lee 1975). Based on trends of pressure recovery on face F2, two different types of flow features within transition regime I have been observed. First, corresponding to α between 4° and 8° and another corresponding to α between 10° and 25° . For α between 4° and 8° , the pressure recovery trend indicated that the suction pressures have been observed to reduce and reach the value of base pressure, whereas in case of α between 10° and 25° , the suction pressures have been observed to reduce significantly and then increase to reach the base pressure. The trend of high localised suction pressures in a portion of face F2 (the region of separation bubble) when compared to face F4, followed by decrease in suction in the remaining portion is corroborative of the reattachment phenomena occurring across the transition regime I (Lee 1975). The zone of high suction on the face F2 immediately after flow separation at corner C2 has been observed to reduce as α changes from 4° to 25° owing to the fact that the point of intermittent reattachment of the shear layers shifts towards the corner C2.

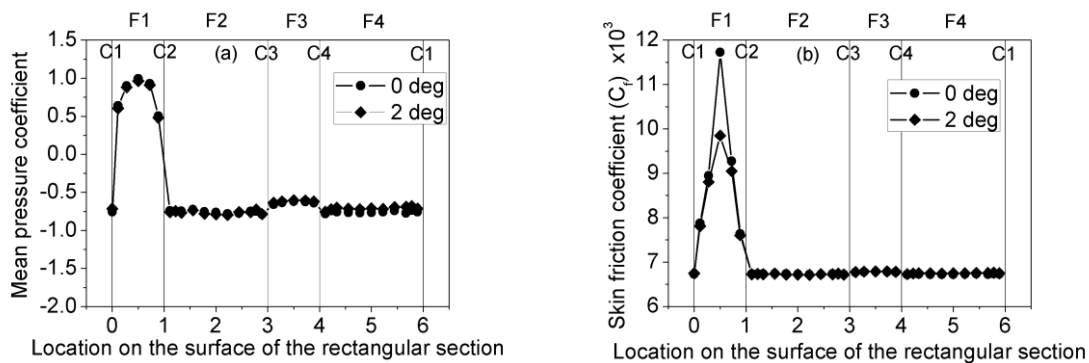


Fig. 6 (a) Mean C_p and (b) C_f distribution for α values in Flow regime I

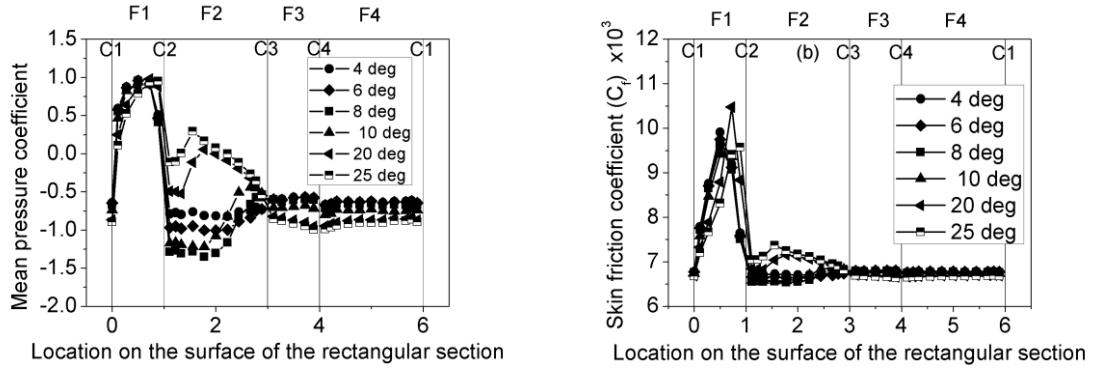


Fig. 7 (a) Mean C_p and (b) C_f distribution for selected α values in transition regime I

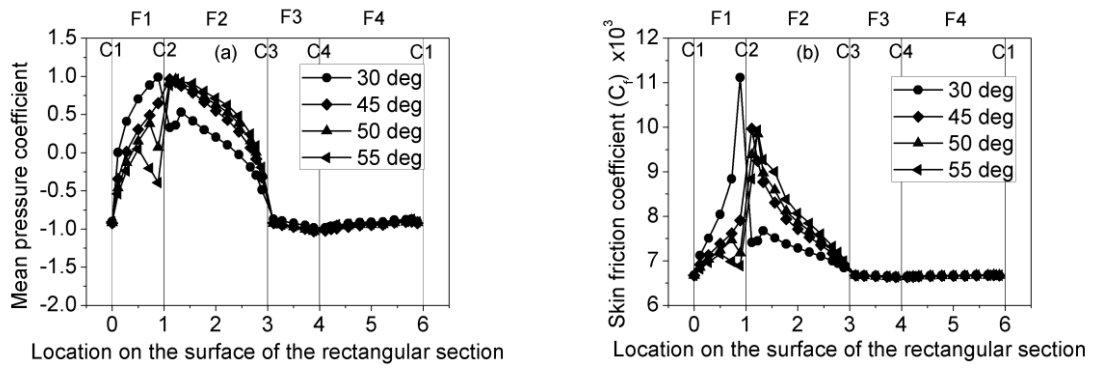


Fig. 8 (a) Mean C_p and (b) C_f distribution for selected α values in Flow regime II

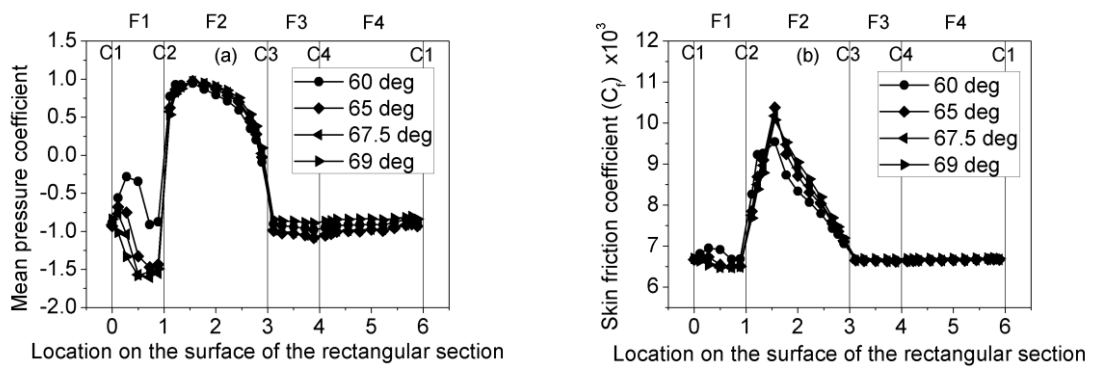


Fig. 9 (a) Mean C_p and (b) C_f distribution for selected α values in transition regime II

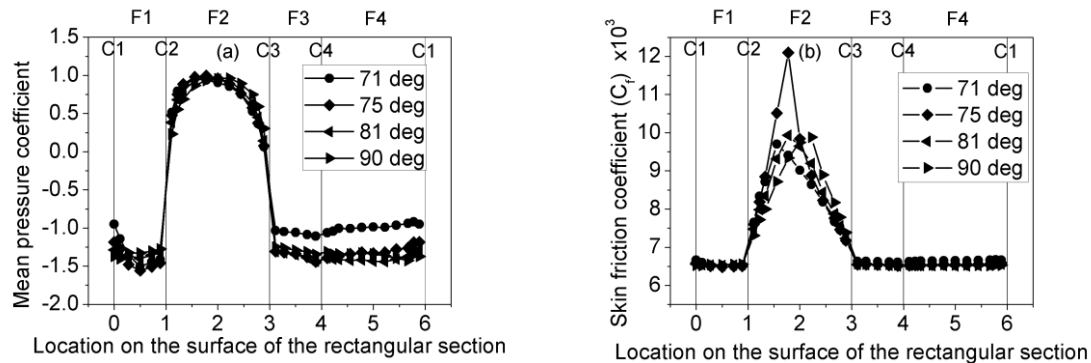


Fig. 10 (a) Mean C_p and (b) C_f distribution for selected α values in Flow regime III

Flow regime II (Fig. 5(c)) involved separation of flow from the corners C1 and C3 of the rectangular section. The rectangular section in this regime is exposed to the oncoming wind in such a way that the flow separation points are distinct and characterized by minimum C_f at corners C1 and C3 for α values of 30° to 55° (Fig. 8(b)). For these values of α , the pressures on faces F1 and F2 are positive, as can be seen in the mean C_p distributions presented in Fig 8 (a).

Transition regime II (Fig. 5(d)) has been observed to be similar to the transition regime I, but for the fact that the shear layers are separated from corners C1 and C3. The shear layers initially separating from corner C2 showed tendency to reattach along face F1, and further move downstream to separate at C1. Since the face F1 is shorter dimension of the rectangular section, the trends of pressure recovery have not been distinctly seen in the mean C_p distributions in the range of α of 60° to 69° (Fig. 9(a)) as those observed in transition regime I. However, for α of 60° , clear trend of pressure recovery in the portion of face F1 between C2 and C3 has been observed. The zone of separation bubble has been observed to be very small compared to that of transition regime I. From Fig. 9(b), the trend of variation of C_f in the face F1 has been observed to be similar to that of face F2 for transition regime I.

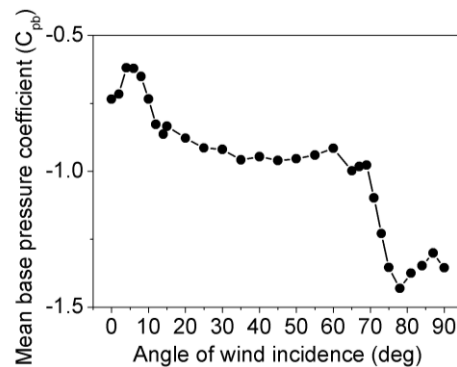
In case of flow regime III (Fig. 5(e)), the shear layers of the flow have been observed to distinctly separate at corners C2 and C3, with significantly high suction pressures in the base pressure region as shown in Fig. 10(a) and minimal C_f at corners C2 and C3 as shown in Fig. 10(b) for α values between 71° and 90° .

The base pressure characterizes the process of entrainment of the fluid flow into the shear layer that grows into a vortex. Hence, its magnitude is indicative of the amount of vortex activity in the wake of the bluff body. Bearman and Trueman (1975) observed that the magnitude of base pressure is higher as the vortex is fully formed farther away from the bluff body. The mean base pressure coefficient (C_{pb}) values have been evaluated based on the average of suction pressures in the regions beyond flow separation, the locations of which have been evaluated based on minima of skin friction coefficient, as discussed earlier. Fig. 11 shows the variation of C_{pb} with α .

The mean C_{pb} has been observed to exhibit comparable magnitudes for α within each of the identified flow regime, which further reinforces the identified flow regimes. Based on the above discussions, the range of angles of wind incidence corresponding to each flow regime have been compiled and presented in Table 2.

Table 2 Identified flow regimes

S. No	Flow regime	Range of α
1	Flow regime I	0° to 2°
2	Transition regime I	4° to 25°
3	Flow regime II	30° to 55°
4	Transition regime II	60° to 69°
5	Flow regime III	71° to 90°

Fig. 11 Variation of mean C_{pb} with angle of wind incidence

3.4 Mean force coefficients and Strouhal number

The variation of mean drag coefficient (C_D^*) with angle of wind incidence (α) has been shown in Fig. 12(a). It has been observed that the present experimental values compared well with the experimental values reported by Hirano *et al.* (2002) for all tested values of α and Larose and D'Auteuil (2008) for α of 0°, 2° and 4°. The mean C_D^* has been observed to reduce from an initial value of 1.43 at 0° to a minimum value of 0.96 at 8°, beyond which it has been observed to increase slightly and become nearly constant value up to 69°. For α between 71° to 81°, steeper increase in mean C_D^* has been observed, beyond which it attained a maximum value 2.1 at α of 90°. The variation of C_D^* has been found to be closely related to the base pressure coefficient, C_{pb} (Fig. 11).

Fig. 12(b) shows the variation of mean lift coefficient (C_L^*) with angle of wind incidence (α). The present experimental values have been observed to compare well with other experimental values reported by Hirano *et al.* (2002), Matsumoto *et al.* (1998) for all values of α and Larose and D'Auteuil (2006) for α less than 10°. The aerodynamic force coefficients reported in literature, which are based on different reference dimensions, have been normalised based on the projected width (normal to the flow direction) as reference dimension prior to comparison. The mean C_L^* values have been observed to be negative up to α of 12° and beyond which the mean C_L^* values have been observed to be positive. The maximum positive and negative mean C_L^* values have been observed to be 0.73 at α of 69° and -0.79 at α of 8°, respectively.

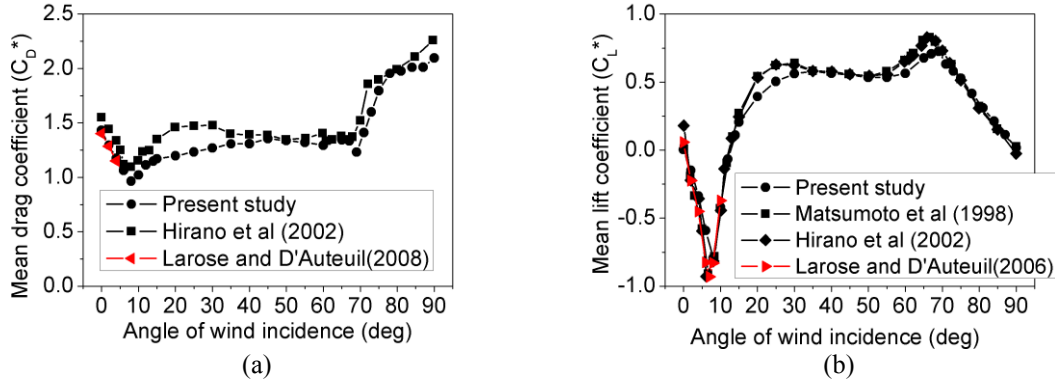


Fig. 12 Variation of (a) mean drag coefficients and (b) mean lift coefficient with α

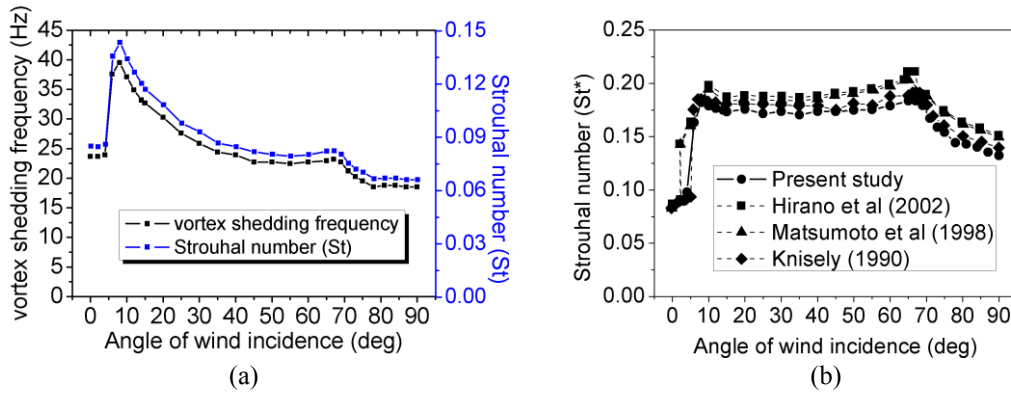


Fig. 13 Variation of (a) St and (b) St^* with angle of wind incidence

Fig. 13(a) shows the variation of vortex shedding frequency (f_s) with α . The maximum value of f_s of 39.55 Hz has been observed at α of 8° (in transition regime I). As mentioned earlier, flow in transition regime I showed tendency of intermittent reattachment, with flow separating from corner C2 reattaching on the face F2 and further separating at corner C3. This phenomenon causes reduction in wake width, because of which, the vortices would be shed more frequently (with reduced distance between fully developed vortices). Beyond 8° , f_s has been observed to reduce up to α of 55° , the range of α corresponding to the identified transition regime I and flow regime II. This could be attributed to increase in wake width in these flow regimes, causing decrease in vortex shedding frequency. For values of α between 60° and 70° , f_s has been observed to be almost constant, beyond which it showed a slightly reducing trend up to α of 81° before taking a constant value in the range of α of 81° to 90° . The minimum value of f_s has been observed to be 18.5 Hz at α of 90° . Fig. 13(a) also shows the variation of St (based on D) with α . The variation of St with α followed the trend of f_s , as expected.

Fig. 13(b) shows the variation of Strouhal number (St^*) based on projected width as reference dimension (Eq. (3)). The values of St^* have been compared with that of the literature. The present experimental values have been observed to be well comparable with the values reported by Knisely

(1990), whereas the values reported by Hirano *et al.* (2000) and Matsumoto *et al.* (1998) have been observed to be slightly higher than the present experimental values by about 10%.

Further, based on the variation of mean force coefficients and Strouhal number with α , critical angle of wind incidence has been observed to be 8° with the following observations:

- (a) steep increase in Strouhal number from 0.08 to 0.14 due to increase in vortex shedding frequency to a maximum value, that also corresponds to a minimum wake width (McClean and Sumner 2014)
- (b) reversal in the slope of the mean lift coefficient, from negative to positive
- (c) minimum value of mean C_D^* (0.96) and maximum value of negative mean C_L^* (-0.79)

3.5 Universal Strouhal number

For a better representation of the mechanism of vortex shedding behind bluff bodies, a concept of universal Strouhal number was suggested in literature based on experimental studies on stationary and oscillating bluff bodies, in addition to conventional Strouhal number. The idea of Universal Strouhal number is that same size vortex sheet may be expected to originate from different bodies, when proper scaling for reference length and velocity is used, besides the vortex shedding frequency (Griffin 1981). Among various proposals in literature, the Universal Strouhal number proposed by Griffin has been considered for comparison with experimental values of the present study. The Griffin's Strouhal number (G) is defined as given below

$$G = \frac{St C_D}{k^3} = \frac{St^* C_D^*}{k^3} \quad \text{or} \quad St C_D = St^* C_D^* = G k^3 \quad (5)$$

where $G=0.073$ as per Griffin (Yeung 2010), St and C_D are the Strouhal number and mean drag coefficient based on D ; the base pressure parameter $k = \sqrt{(1-C_{pb})}$; C_{pb} is the base pressure coefficient.

Fig. 14 shows the variation of G with α . For α between 69° and 90° , the calculated G values have been observed to be between 0.074 and 0.078, which compared well with the reported value of 0.073 ± 0.005 . For α between 6° and 67° , the G values have been observed to be between 0.08 and 0.088, which are slightly higher than the reported value of 0.073 ± 0.005 . However, for values of α less than 6° , the G values have been observed to be less and significantly deviating from the expected range of values. The value of G is directly proportional to the Strouhal number (St^*) as seen in Eq. (5). From Fig. 13(b), the values of St^* are observed to be very less for angles of wind incidence (α) less than 6° , which has resulted in smaller values of G .

Further, the relationship between the product of St and C_D , and the wake parameter 'k' has been investigated, by considering the cubic relationship proposed by Griffin (1981) (Eq. (5)) and the linear relationship proposed by Griffin (1981) (Eq. (6))

$$St C_D = St^* C_D^* = -0.48 + 0.5 k \quad (6)$$

Fig. 15 provides the comparison plot of the product $St C_D$ against the wake parameter 'k' obtained from present experiments and the aforementioned empirical relationships. It has been observed that the data obtained from present experimental study compares well with the linear relationship proposed by Griffin for most of the angles of wind incidence, except for values of α between 0° and 6° (for flow Regime I and a part of transition regime I).

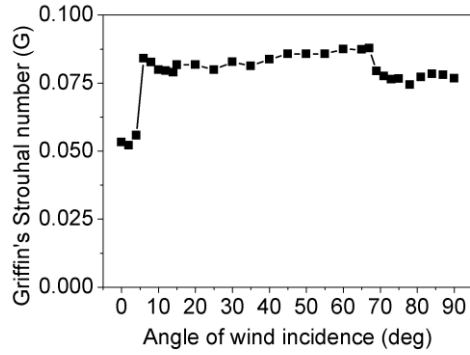


Fig. 14 Variation of Griffin's Strouhal number (G) with angle of wind incidence

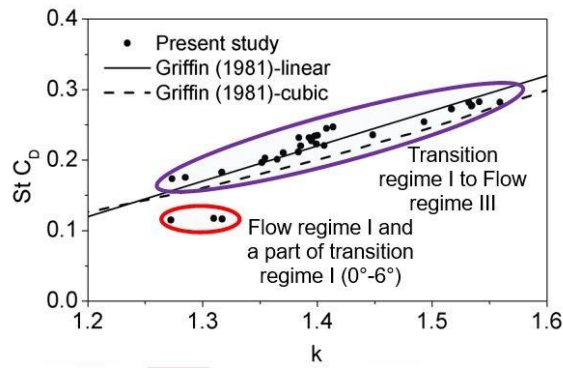


Fig. 15 Plot of $St C_D$ with k

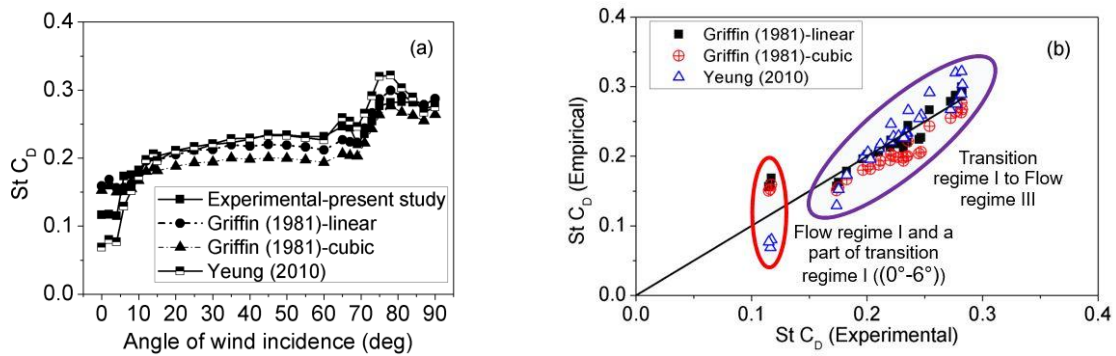


Fig. 16 Comparison of $St C_D$ obtained from the present study with empirical relationships

Further, the relationship among St , C_D and ' k ', as proposed by Yeung (2010) (Eq. (7)) for two-dimensional bluff bodies based on theoretical concept of momentum equation has been considered for comparison.

$$St C_D = k^3 St^* - k St^* \quad (7)$$

Unlike Eqs. (5) and (6), Eq. (7) proposed by Yeung is a function of St^* in addition to ' k ', which changes with angle of wind incidence, as can be seen from Fig. 13(b). Figs. 16(a) and 16(b) compares the product of St and C_D obtained from the present study with those obtained using all the above mentioned empirical relationships as reported in literature.

It can be clearly seen that for values of α between 0° and 6° , the empirically obtained values of $St C_D$ using all three relationships showed significant deviations from the experimental values obtained in the present study. For α corresponding to all the other flow regimes, the empirically obtained $St C_D$ values using Griffin's linear relationship (Eq. (6)) have been observed to be comparing well with the experimental values. Whereas those obtained using cubic relationship (Eq. (5)) have been observed to be comparing well with the experimental values corresponding to the flow regime III (α between 71° and 90°) only and have been observed to be significantly underestimated for flow regime II (α between 30° and 55°). The $St C_D$ values obtained using relationship by Yeung (2010) (Eq. (7)) have been observed to compare well with those corresponding to flow regime II only, and have been observed to be underestimated for flow regime II and overestimated for flow regime III.

It is noteworthy to mention that for values of α between 0° and 6° (for flow Regime I and a part of transition regime I) where significant deviations have been observed, the 2:1 rectangular section is oriented towards the flow in such a way that the ratio of dimension of the rectangular section along the flow to dimension of the rectangular section normal to the flow (R) is greater than 1. Hence, it becomes necessary to check the applicability of the considered empirical relationships to flow regime I, i.e., for rectangular section with $R > 1$, even though the range of ' k ' from the present experiments have been observed to be well within the prescribed range of ' k '. Yeung (2010) presented experimental data from Awbi (1978) on 2-D rectangular cylinders with R values of 0.5, 1 and 1.5, for wind normal to the shorter dimension of the rectangular cylinder to assess the performance of the proposed empirical relationship (Eq. (7)). It was reported by Yeung (2010) that for rectangular sections with B/D less than or equal to 1, the empirically obtained values of $St C_D$ compared well with the experimental values, whereas discussions on rectangular section with $R=1.5$ have not been highlighted. In the present study, the performance assessment of Eq. (7) has been extended for 2-D rectangular cylinders with R value of 2, 3, 4 and 5, based on the data obtained from Awbi (1978). The values of St^* required for substitution in Eq. (7) have been suitably obtained from Awbi (1978). Fig. 17 shows the comparison of $St C_D$ and ' k ' from experiments and Yeung's relationship. The experimental values from the present study for $\alpha=0^\circ$ has been included in the plot corresponding to $R=2$. For $R=3$, two values of St have been provided corresponding to two values of Reynolds number, as sudden change in St due to flow reattachment with change in Reynolds number (Awbi 1978) has been reported. Both values have been considered for comparison.

It can be seen from Fig. 17 that for higher values of R , the experimental data has been observed to show significant deviation with respect to the empirical relationship proposed by Yeung (2010). Similar deviation has been observed in case of Griffin's linear and cubic relationships also (Fig. 18) for rectangular sections with R greater than 1. Hence, more detailed investigations on the Universality of Strouhal number for such shapes involving long afterbodies are required.

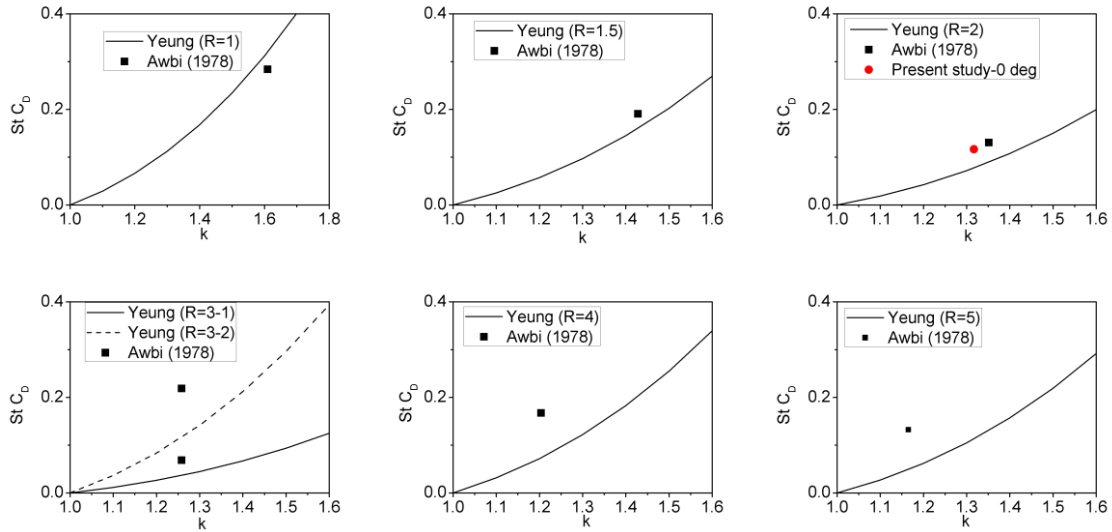


Fig. 17 Comparison of Yeung's relationship for 2-D rectangles with R of 1 to 5

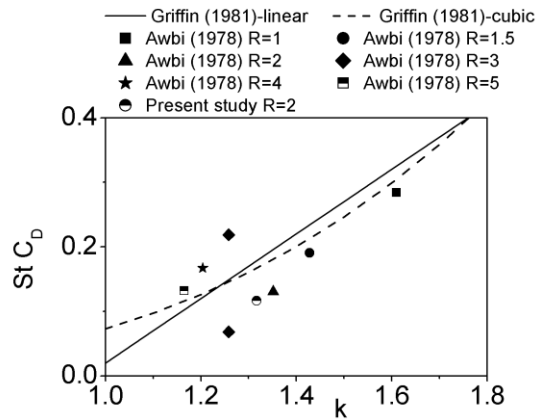


Fig. 18 Variation of Griffin's Strouhal number (G) with angle of wind incidence

3.6 Spectra of aerodynamic force coefficients

The variation of root mean square (r.m.s) of fluctuating components of drag and lift force coefficients with α have been shown in Fig. 19. Minimum value of r.m.s fluctuating component of lift force coefficient of 0.13 has been observed at critical angle of wind incidence of 8° , whereas maximum value of 0.69 has been observed at α of 78° . Significant change in trend of r.m.s fluctuating components of C_L^* has been observed to occur predominantly in flow regimes I and III, whereas r.m.s fluctuating components of C_D^* changed prominently in flow regime III. The spectrum of C_D^* and C_L^* for typical angles of wind incidence have been presented in Fig. 20.

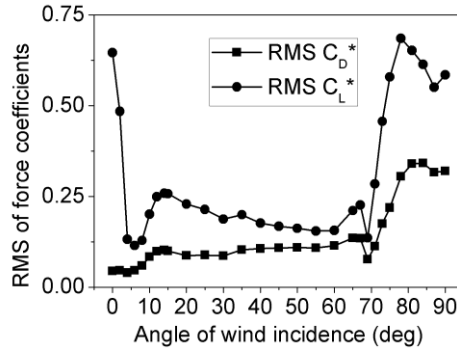


Fig. 19 Variation of r.m.s of force coefficients with angle of wind incidence

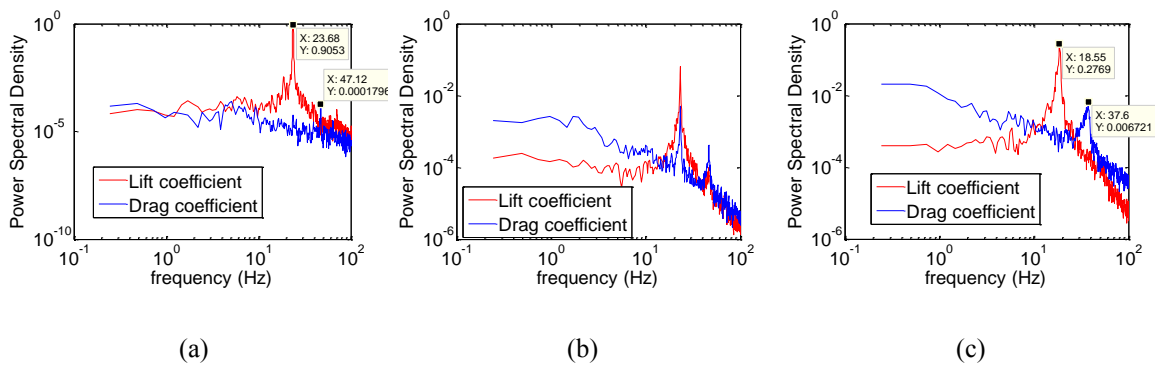


Fig. 20 Spectra of the lift and drag coefficients for (a) $\alpha=0^\circ$, (b) $\alpha=67^\circ$ and (c) $\alpha=90^\circ$

For wind normal to one of the faces of the rectangular section, i.e., α of 0° (Fig. 20(a)) and 90° (Fig. 20(c)), the spectrum of C_L^* has been observed to have distinct peak corresponding to the vortex shedding frequency, whereas the spectrum of C_D^* has been observed to have distinct peak corresponding to twice the vortex shedding frequency. For 0° , since the value of r.m.s fluctuating component of C_D^* is significantly less than the value of r.m.s fluctuating component of C_L^* , the peak corresponding to the spectra of C_D^* at twice the vortex shedding frequency has not been distinctly seen in the Fig. 20(a). The occurrence of distinct peaks in the spectrum of C_D^* and C_L^* are indicative of the fact that only opposite faces of the rectangular section normal the flow direction contribute to the drag forces, while opposite faces of the rectangular section along to the flow direction contribute to the lift forces. For oblique wind angle of 67° (Fig. 20 (b)), both the spectrum of C_D^* and C_L^* have been observed to have two peaks, one corresponding to f_s and another corresponding to twice f_s , which is indicative of the fact that all the faces of the rectangular section contribute to both drag and lift forces. Similar behavior has been observed for all other oblique angles of wind incidence.

4. Spatio-temporal analysis of measured pressures using POD

Traditional statistical analysis of measured fluctuating pressures alone would not suffice the physical interpretation of the aerodynamic effects of complex flow mechanisms on the bluff bodies. Spatio-temporal analysis of the fluctuating pressures helps in isolating the correlated fluctuating pressures caused by different flow mechanisms. Spatio-temporal correlations can be better studied with the aid of advanced stochastic methods like POD (Qiu *et al.* 2014). In order to better understand the influence of complex flow phenomena on the surface pressures of the 2:1 rectangular section, POD analysis of the measured randomly fluctuating pressure field acting on the surface of the rectangular section has been carried out.

POD technique has also been referred by various other names, viz, covariance proper transformation (CPT) or Principal Component Analysis (PCA) in literature (de Grenet and Ricciardelli 2004, Carassale 2012). A brief description of the procedural aspects of POD for the pressure field has been presented here.

The measured unsteady pressure field can be expressed as

$$p(x, y, t) = \bar{p}(x, y) + p'(x, y, t) \quad (8)$$

where \bar{p} is the mean pressure; and p' is the fluctuating pressure. POD represents multi-variate random fluctuating pressure field p' as a sum of the products of deterministic, uncorrelated, orthogonal distributions of the field variable called POD modes ($\Phi_m(x, y)$) and random coefficients called principal co-ordinates/POD co-ordinates ($a_m(t)$).

$$p'(x, y, t) = a(t) \Phi(x, y) = \sum_{m=1}^M a_m(t) \Phi_m(x, y) \quad (9)$$

Hence, with respect to the pressure data, POD can be potentially seen as a technique to separate space and time components in the fluctuating pressure data (Li *et al.* 2012). The deterministic coordinate function $\Phi(x, y)$ in Eq. (9) optimally maximizes the projection of the randomly fluctuating wind pressure field $p'(x, y, t)$, to itself in a mean square sense. Upon this maximality criterion, the projection is transformed to an eigen value problem, and can be written as

$$\iint T(x, y, x', y') \Phi(x', y') dx' dy' = \lambda \Phi(x, y) \quad (10)$$

where $T(x, y, x', y')$ is a spatial correlation of the fluctuating pressure field. The fluctuating pressure field, given discretely at M points, can be rewritten in the matrix form as

$$T \Phi = \lambda \Phi \quad (11)$$

where T is the spatial correlation matrix of the fluctuating wind pressure field of size $M \times M$, and is real symmetric and positive definite in nature. Φ is the space function that contains a series of M orthogonal eigen vectors/POD modes ($\Phi_m(x, y)$) arranged in the decreasing order of the eigen values of the zero-time lag covariance matrix T of $p'(x, y, t)$. λ is the diagonal matrix of the eigen values of T (principal coordinates). The evaluated principal coordinates/eigen values (λ_i) denote the relative contribution of each mode to the fluctuating pressure field. These eigen values can be normalized with the cumulative sum of eigen values of the system, and are defined as $\lambda_{i, norm}$.

By the inclusion of the mean component of pressure data for POD analysis, distortion of POD

modes and variations in energy distribution per mode have been observed (Tamura *et al.* 1999). In the present study, time-averaged mean pressure values have been subtracted from the measured pressure data. Subsequently, POD analysis of the measured fluctuating pressures has been carried out for all the angles of wind incidence. Very limited literature has dealt with the POD analysis for wind flows around rectangular sections for angles of wind incidence, which are oblique to the faces. In the present study, the applicability of the POD technique for capturing change in aerodynamic signature with angle of wind incidence has been studied. For the sake of brevity, results pertaining to limited angles of incidence, covering all the identified flow regimes have been presented.

4.1 Eigen values and mode shapes

The normalized eigen values and their cumulative sum for selected angles of wind incidence have been presented in Table 3. It is to be noted that the normalized eigen values correspond to the proportion of energy (in %) associated with each POD mode, with respect to the total energy of the system. Hence, most energetic POD mode is considered to be corresponding to the dominant flow field. This energy of every mode gives information about the percentage of variance of the overall aerodynamic pressures acting on the rectangular section. For α of 0° , which corresponds to flow regime I, the first and second POD modes captured 80.96% and 7.25% of the total variance of the process, respectively. Similar values have been observed for α of 2° in the same flow regime. Whereas for α of 4° in the transition regime I, the first and second POD modes constituted 36.97% and 21.23% of the total variance of the process. There is significant reduction in the energy content pertaining to the first POD mode, as the complexity in the flow around bluff body increases due to transition in the flow regime, for α of 4° to 8° . Further, in these flow regimes, the flow behavior around the rectangular section has been observed to be similar to that of elongated rectangles, where contribution of more than one POD mode has been reported (Hoa *et al.* 2013). Within transition regime I, two kinds of pressure recovery have been observed, one from α of 4° to 8° and another from 10° to 25° as highlighted earlier (Fig. 7(a)). Beyond critical angle of wind incidence of 8° in transition regime I, increase in eigen value associated with first mode from about 37% (for α of 4° to 8°) to 55% has been observed. Similar distributions of energy content of POD modes within flow regime II, transition regime II and flow regime III can be seen from the Table 3. The sum of first three POD modes have been observed to constitute to most of the energy (about 92%) contained in the pressure field for almost all values of α , except for α of 4° to 8° for which more number of POD modes have been observed to be required.

The first four POD mode shapes superimposed on the geometry of rectangular section have been shown in Fig. 21(a) to 21(e) for α of 0° , 8° , 35° , 67° and 90° respectively, as representative of the identified flow regimes. Same scaling factor has been adopted for all the mode shapes presented. For all the angles of wind incidence, the mode shape of the pressure fluctuations on the windward face(s) have been observed to be significantly negligible in comparison to all other three faces. This is due to the fact that the windward face(s) are subjected to uniform and smooth flow with very low turbulence intensity. The mode shapes corresponding to wind flow normal to any one of the faces (α of 0° and 90°) have been found to exhibit either symmetric or anti-symmetric pattern.

For α of 0° in flow regime I (Fig. 21(a)), the first and second POD mode exhibited anti-symmetric pattern. The mode shape on one half of leeward face (face F3) has been observed to be completely out-of-phase in comparison to the other half of the leeward face, while the mode shape on the side faces F2 and F4 have been observed to be similar and in-phase, with fully correlated across each of the faces. However, third and fourth POD modes exhibited symmetric pattern. The mode shape

across F3 were completely in phase and fully correlated, also showing similarity to the mean pressure distribution in the face F3 (Fig. 4). For values of α in transition regime I and transition regime II (Figs. 21(b) and 21(c)), the mode shape on the face of the rectangular section where the transition phenomenon has been identified to occur (face F2 for transition regime I and face F1 for transition regime II) has been found to be of complex nature, with more number of inflection points when compared to other flow regimes. For α of 90° in flow regime III (Fig. 21(e)), the first and fourth POD modes exhibited anti-symmetry, while second and third POD modes exhibited symmetry.

Among the second and third POD modes, which exhibited symmetry, second POD mode has mode shape across its leeward face (face F4) similar to mean pressure distribution on the same face.

Table 3 Eigen values and their cumulative sum for selected α

α (deg)	Flow regime	Eigen Value (%) (λ)	POD mode number						
			1	2	3	4	5	6	7-32
0	Flow regime I	$\lambda_{i,norm}$	80.96	7.25	4.40	2.00	1.28	0.79	3.30
		$\lambda_{i,cum}$	80.96	88.22	92.62	94.62	95.90	96.70	100
2	Flow regime I	$\lambda_{i,norm}$	77.42	7.32	6.62	2.29	1.66	0.90	3.78
		$\lambda_{i,cum}$	77.42	84.74	91.36	93.65	95.32	96.22	100
4	Transition regime I	$\lambda_{i,norm}$	36.97	21.23	14.34	8.24	4.09	3.37	11.77
		$\lambda_{i,cum}$	36.97	58.20	72.54	80.78	84.87	88.23	100
6	Transition regime I	$\lambda_{i,norm}$	34.21	19.59	13.02	11.70	5.65	3.17	12.67
		$\lambda_{i,cum}$	34.21	53.80	66.81	78.51	84.16	87.33	100
8	Transition regime I	$\lambda_{i,norm}$	33.45	21.05	11.34	9.39	6.15	4.06	14.56
		$\lambda_{i,cum}$	33.45	54.51	65.84	75.23	81.38	85.44	100
15	Transition regime I	$\lambda_{i,norm}$	62.34	14.05	10.78	2.54	1.70	1.52	7.08
		$\lambda_{i,cum}$	62.34	76.38	87.16	89.70	91.40	92.92	100
25	Transition regime I	$\lambda_{i,norm}$	55.92	24.75	9.41	4.01	1.09	1.01	3.80
		$\lambda_{i,cum}$	55.92	80.67	90.08	94.09	95.19	96.20	100
30	Flow regime II	$\lambda_{i,norm}$	52.19	30.31	8.60	4.12	1.12	0.74	2.92
		$\lambda_{i,cum}$	52.19	82.50	91.10	95.23	96.35	97.08	100
45	Flow regime II	$\lambda_{i,norm}$	43.13	41.47	8.62	2.47	1.40	0.61	2.30
		$\lambda_{i,cum}$	43.13	84.60	93.23	95.69	97.09	97.70	100
55	Flow regime II	$\lambda_{i,norm}$	44.77	38.01	8.39	2.13	1.80	1.53	3.37
		$\lambda_{i,cum}$	44.77	82.79	91.17	93.30	95.10	96.63	100
60	Transition regime II	$\lambda_{i,norm}$	44.45	38.82	7.78	2.08	1.62	1.28	3.98
		$\lambda_{i,cum}$	44.45	83.27	91.05	93.13	94.74	96.03	100
67	Transition regime II	$\lambda_{i,norm}$	58.17	21.35	8.34	3.16	1.94	1.50	5.55
		$\lambda_{i,cum}$	58.17	79.52	87.86	91.02	92.95	94.45	100
71	Flow regime III	$\lambda_{i,norm}$	68.56	16.44	4.60	3.69	1.79	1.56	3.36
		$\lambda_{i,cum}$	68.56	85.01	89.60	93.29	95.08	96.64	100
81	Flow regime III	$\lambda_{i,norm}$	68.97	16.79	5.09	3.94	1.81	0.92	2.48
		$\lambda_{i,cum}$	68.97	85.76	90.85	94.79	96.60	97.52	100
90	Flow regime III	$\lambda_{i,norm}$	69.84	16.43	5.27	3.90	1.43	0.81	2.33
		$\lambda_{i,cum}$	69.84	86.27	91.54	95.44	96.87	97.67	100

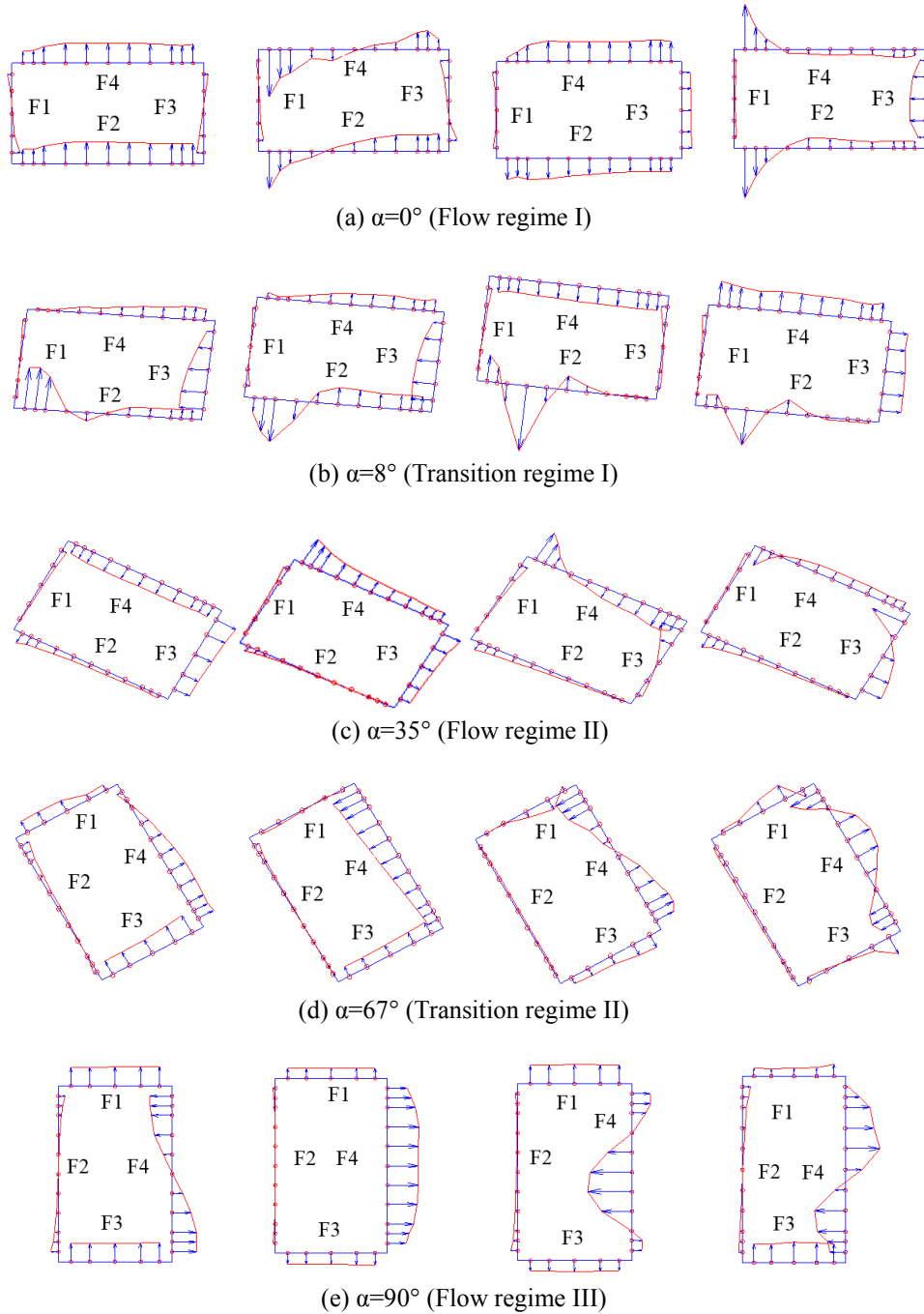


Fig. 21 First four mode shapes for (a) $\alpha=0^\circ$, (b) $\alpha=8^\circ$, (c) $\alpha=35^\circ$ and (d) $\alpha=67^\circ$ (e) 90°

4.2 Contribution of POD modes to aerodynamic forces

In order to identify the contribution of each individual POD modes to different aerodynamic forces, viz, drag and lift components, fluctuating aerodynamic drag and lift coefficients associated with each individual POD mode have been evaluated (de Grenet and Ricciardelli 2004). The ratio of variance of evaluated aerodynamic coefficients corresponding to an individual POD mode (based on reconstructed time series of pressures) to variance of the evaluated total aerodynamic coefficients have been computed and presented in Table 4. It indicates that every individual POD mode associates with anyone or both the aerodynamic forces.

Table 4 Contribution of POD modes to drag and lift force coefficients

α (deg)	Flow regime	Force component	POD mode number						
			1	2	3	4	5	6	7-32
0	Flow regime I	Drag	0	0.01	12.12	10.35	68.15	0.00	9.37
		Lift	99.93	0.05	0.01	0	0	0	0.01
2	Flow regime I	Drag	21.30	4.08	5.72	11.64	45.43	4.94	6.90
		Lift	99.91	0.03	0.03	0	0	0	0.02
4	Transition regime I	Drag	0	21.50	21.96	38.30	11.41	0.04	6.80
		Lift	66.75	30.35	2.18	0.39	0.01	0.01	0.31
6	Transition regime I	Drag	0	1.50	68.44	11.85	13.30	0.15	4.76
		Lift	60.02	1.08	0.10	37.90	0.18	0.48	0.24
8	Transition regime I	Drag	32.42	30.43	1.30	26.11	0	0.02	9.72
		Lift	59.36	10.49	17.12	9.10	0.36	0.49	3.08
15	Transition regime I	Drag	53.68	28.97	14.37	0.97	0.02	0.02	1.97
		Lift	91.65	5.93	1.51	0.44	0	0.10	0.38
25	Transition regime I	Drag	9.08	82.82	4.87	0.67	0.19	0.09	2.29
		Lift	91.74	6.64	1.26	0.12	0.02	0.03	0.19
45	Flow regime II	Drag	6.00	89.98	2.37	0.13	0.02	0.04	1.47
		Lift	69.33	30.16	0.25	0.13	0	0.00	0.12
60	Transition regime II	Drag	9.45	87.48	0.64	0.04	0.73	0.09	1.56
		Lift	65.88	33.45	0.38	0.06	0.01	0.10	0.12
67	Transition regime II	Drag	16.25	78.03	2.63	0.08	1.25	0.35	1.41
		Lift	98.19	0.07	1.38	0	0.25	0.01	0.08
71	Flow regime III	Drag	8.59	62.68	13.46	14.13	0.02	0.02	1.11
		Lift	98.55	0.68	0.50	0.19	0.01	0.06	0.03
81	Flow regime III	Drag	0.00	89.78	6.56	0.48	2.88	0.01	0.29
		Lift	97.08	0.96	0	1.87	0.03	0.05	0.02
90	Flow regime III	Drag	0.32	91.60	6.21	0.44	1.12	0	0.30
		Lift	96.86	0.03	0.33	2.66	0	0.10	0.01

For all the values of α , the first POD mode was predominantly contributing to the fluctuating lift force, and it had the frequency characteristics corresponding to the physical phenomena of vortex shedding frequency. This could be attributed to the fact that the predominant loading mechanism in this particular case of rectangular section is due to periodic shedding of Karman vortices. It is to be noted that the number of POD modes required to accurately construct the time histories of force coefficients, and subsequently the spectra has been observed to vary from case to case. However, dominance of first and second POD mode, as observed in the present study has been more widely reported in the literature as they have dominant eigen value of the overall process and also from the aspects of obtaining generalized and simplified equivalent static wind loads on structures.

Similarities in the contribution of individual POD modes to lift force coefficient have been observed within each flow regime, except for a few values of α adjacent to transition regimes. In the flow regime I, the first POD mode predominantly contributed to the fluctuating lift force with about 99.93% to the total variance of lift force coefficient.

In case of transition regime I, for the range of α between 4° and 8° , two POD modes have been observed to contribute significantly to the fluctuating lift force (twin POD mode dominant) whereas for the range of α between 10° and 25° , the contribution to lift force coefficient has been observed to be single mode dominant. Further, flow regime II and transition regime II have been observed to be twin POD mode dominant. Whereas flow regime III has been observed to be single POD mode dominant by means of its contribution to lift force coefficient.

The r.m.s fluctuating component of drag force coefficient (Fig. 19) was observed to be less for values of α between 0° and 15° , as well as for α of 69° and 71° . Hence, for these values of α , contribution of POD modes to the variance of drag force coefficient has been observed to be distributed across higher POD modes, which do not have significant eigen values (Table 3) associated with them. For α of 0° , the major contribution to the variance of C_D^* was from fifth POD mode (with $\lambda=1.28\%$), which contributed 68.15% of the variance of drag force coefficient. For α of 8° , fourth POD mode (with $\lambda=9.39\%$) contributed 26.11% of the variance of C_D^* . Similar pattern of contribution of higher POD modes to the variance of drag force component has been observed (de Grenet and Ricciardelli 2004) based on the POD analysis of fluctuating pressures on 2D square cylinders in tandem arrangement for a set of spacing (with closer spacing) where the flow behavior is similar to that of an elongated rectangular section. Beyond α of 15° (except α of 69° and 71°), it has been observed that the second POD mode is predominantly contributing to the fluctuating drag force coefficient, by capturing more than about 80% of the variance of C_D^* . In flow regime II, the second POD mode contributed to both the variance of C_L^* and the variance of C_D^* . Such contribution of one POD mode to both components of aerodynamic forces have also been reported in literature (de Grenet and Ricciardelli 2004).

Figs. 22 and 23 present the comparison of time histories and spectrum of experimentally evaluated lift force coefficient with those reconstructed based on first and second POD modes individually for twin POD mode dominant ($\alpha=8^\circ$) and single POD mode dominant ($\alpha=0^\circ$) case of α , respectively. In case of twin POD mode dominated cases of α (Fig. 22), the time histories of lift coefficients reconstructed from individual POD modes have been observed to show differences with respect to that of experiments with the contribution of first two POD modes to the variance of lift coefficient by about 65% and 30%, respectively. In case of spectrum, good comparison of spectrum obtained based on reconstructed time histories from POD modes in the high frequency region has been observed, thereby preserving the frequency peaks corresponding to vortex shedding. The major difference in the spectrum has been observed in the low frequency range of 0.3 to 10 Hz. Similar trend of deviation in spectrum of reconstructed pressures at individual pressure taps have been

observed on 2-D square section by Hoa *et al.* (2013).

For single POD dominated cases of α (Fig. 23), good comparison of experimental and reconstructed time histories and spectrum based on first POD mode have been observed for all the values of α .

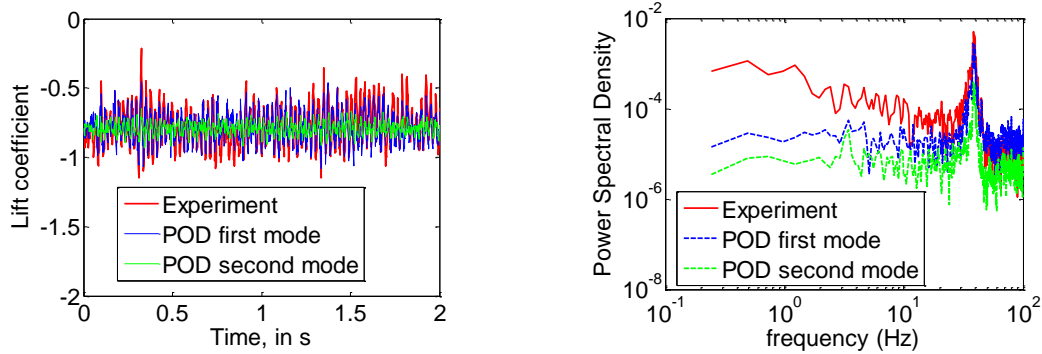


Fig. 22 Comparison of time history and spectra of lift coefficients of experimental and POD based reconstructed for $\alpha = 8^\circ$ (twin mode dominant)

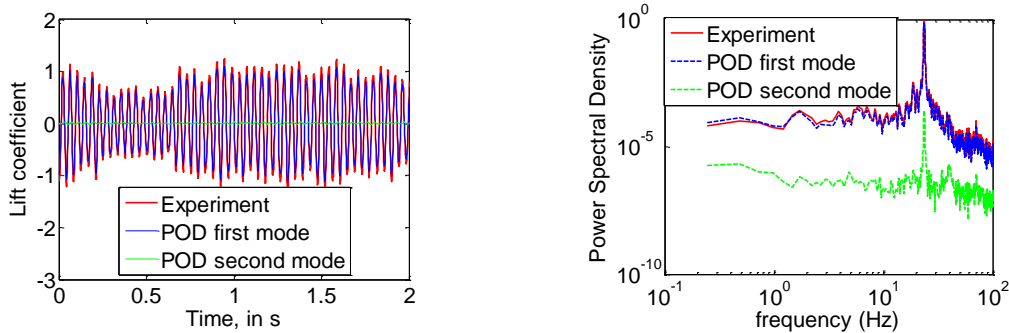


Fig. 23 Comparison of time history and spectra of lift coefficients of experimental and POD based reconstructed for $\alpha = 0^\circ$ (single mode dominant)

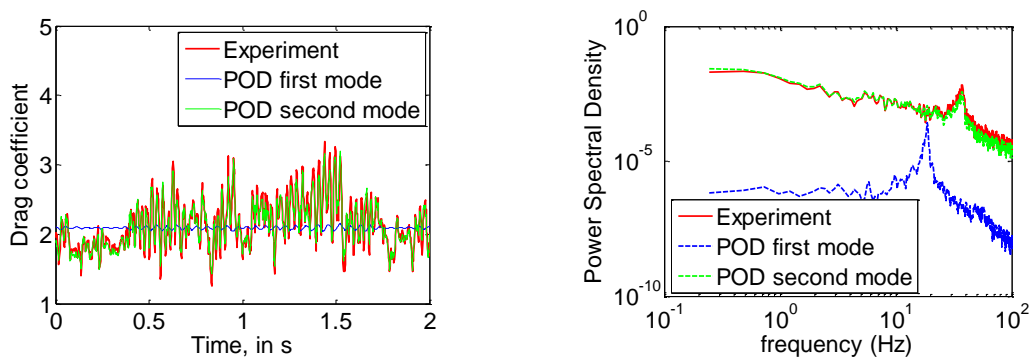


Fig. 24 Comparison of time history and spectra of drag coefficients of experimental and POD based reconstructed for $\alpha = 90^\circ$

Fig. 24 presents the comparison of time histories and spectrum of experimentally evaluated drag force coefficient and that reconstructed based on first and second POD modes individually for a typical value of α of 90° . Similar to the time history and spectrum of lift force coefficient for single mode dominant cases of α , good agreement in experimental and reconstructed time histories and spectrum based on first POD mode have been observed.

5. Conclusions

The effect of angle of wind incidence on the aerodynamic characteristics of a 2:1 rectangular section has been studied based on wind tunnel pressure measurement studies carried out under uniform and smooth inflow conditions. Based on the change in positions of separation of shear layers emanating from the rectangular section at various angles of wind incidence, the distributions of mean pressure coefficients and empirically evaluated skin friction coefficient, three flow regimes along with two transition regimes have been identified. The characteristics of the flow in each of the identified flow regimes have been brought out. The critical angle of wind incidence has been observed to be 8° , as it is associated with significant increase in Strouhal number and reversal of slope of mean lift coefficient. The maximum positive and negative values of the mean aerodynamic lift coefficients have been observed to be at oblique angles of wind incidence, thus re-emphasizing the need to study the effect of angle of wind incidence.

The relationship between Strouhal number (St^*), mean drag coefficient (C_D^*) and the base pressure parameter ' k ', in the form of Universal Strouhal number expressions has been studied based on the experimental data. Among the three relationships considered, the linear relationship proposed by Griffin (1981) has been observed to better represent the relationship between St , C_D and ' k ' for 2:1 rectangular section considered in the present study for most of the values of α , except for values of α between 0° and 8° . For these angles of wind incidence, the afterbody portion of the rectangular section has been observed to be longer than those for other angles of wind incidence. The performance limitation of the empirical relationships, especially for elongated rectangular sections with wind normal to the shorter dimension have been studied further. It has been inferred from the observed deviations that further studies on Universal Strouhal number are required for such cases. Similar observation has been made by Csiba and Martinuzzi (2008), where effect of unequal strength shear layers has been studied on triangular section at various angles of wind incidence.

Based on the POD analysis of the measured fluctuating pressures on the 2:1 rectangular section for various angles of wind incidence, the eigen values corresponding to the first POD mode (that is representative of the largest possible/most dominant variance of the stochastic pressure field) were observed to be comparable within every flow regime, which corroborates the classification of the earlier identified flow regimes. Limited number of POD modes have been observed to be sufficient to represent the physical phenomenon, without loss in predominant frequency components. The ratio of variance of aerodynamic force coefficients obtained from pressure traces reconstructed from individual POD modes to the variance of the total aerodynamic force coefficient have been shown to quantify the percentage of contribution of individual POD mode to the drag and lift forces. For all the values of α , the first POD mode has been observed to contribute mainly to the fluctuating lift force coefficient. For α values beyond 25° , the second POD mode has been observed to contribute mainly to the fluctuating drag force coefficient.

The scope of the present study is limited to the aerodynamic characteristics of 2:1 rectangular section under uniform, smooth flow at a Reynolds number of 0.6×10^5 . Further, the identification of flow regimes in the present study is based on the variations of mean pressure coefficient and skin friction coefficient evaluated from synchronous pressure measurements on the surface of the rectangular section. Hence, detailed investigations using advanced flow visualization techniques like Particle Image Velocimetry (PIV) will be required to validate the identified flow regimes. The range of angles of wind incidence corresponding to the identified flow regimes may vary depending up on Reynolds number, which needs to be further investigated. This is because of the pronounced Reynolds number effects on aerodynamics of rectangular sections at oblique angles of wind incidence as reported in literature (Larose and D'Auteuil 2008, Schewe 2009).

Acknowledgments

This paper is being published with the kind permission of Director, CSIR-Structural Engineering Research Centre, Chennai, India. The support rendered by the technical and non-technical staff of the Wind Engineering Laboratory of CSIR-SERC is gratefully acknowledged. The authors would like to thank the reviewers for their valuable feedback.

References

- Ahlborn, B., Setob, M.L. and Noack, B.R. (2002), "On drag, strouhal number and vortex-street structure", *Fluid Dyn Res.*, **30**(6), 379-399.
- Amrouche, N., Dizene, R. and Laneville, A. (2010), "Observations of the wind tunnel blockage effects on the mean pressure distributions around rectangular prisms in smooth and grid turbulent flows", *Revue des Energies Renouvelables SMEE'10*, Algeria, 21-26.
- Awbi, H.B. (1978), "Wind-tunnel-wall constraint on two-dimensional rectangular-section prisms", *J. Wind. Eng. Ind. Aerod.*, **3**(4), 285-306.
- Bartoli, G., Bruno, L., Buresti, G., Ricciardelli, F., Salvetti, M.V. and Zasso, A. (2009), "BARC: a benchmark on the aerodynamics of a rectangular 5:1 cylinder", *Proceedings of the 5th European African Conference on Wind Engineering*, Italy, July.
- Bruno, L., Fransos, D., Coste, N. and Bosco, A. (2010), "3D flow around a rectangular cylinder: A computational study", *J. Wind. Eng. Ind. Aerod.*, **98** (6-7), 263-276.
- Bruno, L., Salvetti, M.V. and Ricciardelli, F. (2014), "Benchmark on the aerodynamics of a rectangular 5:1 cylinder: An overview after the first four years of activity", *J. Wind. Eng. Ind. Aerod.*, **126**, 87-106.
- Carassale, L. (2012), "Analysis of aerodynamic pressure measurements by dynamic coherent structures", *Probabilist. Eng. Mech.*, **28**, 66-74.
- Carassale, L., Solari, G. and Tubino, F. (2007), "Proper orthogonal decomposition in wind engineering: part 2: theoretical aspects and some applications", *Wind Struct.*, **10**(2), 177-208.
- Cebeci, T., Mosinskis, G.J. and Smith, A.M. O. (1972), "Calculation of separation points in incompressible turbulent flows", *J. Aircraft.*, **9**(9), 618-624.
- Csiba, A.L. and Martinuzzi, R.J. (2008), "Investigation of bluff body asymmetry on the properties of vortex shedding", *J. Wind. Eng. Ind. Aerod.*, **96**, 1152-1163.
- de Grenet, E. T. and Ricciardelli, F. (2004), "Analysis of the wind loading of square cylinders using covariance proper transformation", *Wind Struct.*, **7**(2), 71-88.
- Dutta, S., Muralidhar, K. and Panigrahi, P. (2003), "Influence of the orientation of a square cylinder on the

- wake properties”, *Exp. Fluids.*, **34**(1), 16-23.
- Gao, G. and Zhu, L. (2016), “Measurement and verification of unsteady galloping force on a rectangular 2:1 cylinder”, *J. Wind. Eng. Ind. Aerod.*, **157**, 76-94.
- Griffin, O.M. (1981), “Universal similarity in the wakes of stationary and vibrating bluff structures”, *T. Am. Soc. Mech. Eng.*, **103**, 52-58.
- Hemon, P. and Santi, F. (2002), “On the aeroelastic behavior of rectangular cylinders in cross-flow”, *J. Fluid. Struct.*, **16**(7), 855-889.
- Hemon, P., Santi, F., Schnoerringer, B. and Wojciechowski, J. (2001), “Influence of free-stream turbulence on the movement-induced vibrations of an elongated rectangular cylinder in cross-flow”, *J. Wind. Eng. Ind. Aerod.*, **89**, 1383-1395.
- Hirano, H., Maruoka, A. and Watanabe, S. (2002), “Calculation of aerodynamic properties of rectangular cylinder with slenderness ratio of 2:1 under various angles of wind incidence”, *J. Struct. Eng.*, **48**, 971-978.
- Hoa, L. T., Tamura, Y., Matsumoto, M. and Shirato, H. (2013), “Understanding of unsteady pressure fields on prisms based on covariance and spectral proper orthogonal decompositions”, *Wind Struct.*, **16**(5), 517-540.
- Keerthana, M. and Harikrishna, P. (2013). “Application of CFD for assessment of galloping stability of rectangular and H sections”, *J. Sci. Ind. Res. India*, **72**, 419-427.
- Kikuchi, H., Tamura, Y., Ueda, H. and Hibi, K. (1997), “Dynamic wind pressure acting on a tall building model – proper orthogonal decomposition”, *J. Wind. Eng. Ind. Aerod.*, **69-71**, 631-46.
- Knisely, C. (1990), “Strouhal numbers of rectangular cylinders at incidence: A review and new data”, *J. Fluid. Struct.*, **4** (4), 371-393.
- Larose, G.L. and D’Auteuil, A. (2006), “On the Reynolds number sensitivity of the aerodynamics of bluff bodies with sharp edges”, *J. Wind. Eng. Ind. Aerod.*, **94**, 365-376.
- Larose, G.L. and D’Auteuil, A. (2008), “Experiments on 2D rectangular prisms at high Reynolds numbers in a pressurised wind tunnel”, *J. Wind. Eng. Ind. Aerod.*, **96**, 923-933.
- Lee, B.E. (1975), “The effect of turbulence on the pressure field of a square prism”, *J. Fluid. Mech.*, **69**, 263-282.
- Li, F., Gu, M., Ni, Z. and Shen, S. (2012), “Wind pressures on structures by proper orthogonal decomposition”, *J. Civil Eng. Architect.*, **6**(2), 238-243.
- Mannini, C., Marra, A.M., Pigolotti, L. and Bartoli, G. (2017), “The effects of turbulence and angle of attack on the aerodynamics of a cylinder with rectangular 5:1 cross-section”, *J. Wind. Eng. Ind. Aerod.*, **161**, 42-58.
- Matsumoto, M., Ishizaki, H., Matsuoka, C., Daito, Y., Ichikawa, Y. and Shimahara, A. (1998), “Aerodynamic effects of the angle of wind incidence on a rectangular prism”, *J. Wind. Eng. Ind. Aerod.*, **77-78**, 531-542.
- McClellan, J.F. and Sumner, D. (2014), “An experimental investigation of aspect ratio and incidence angle effects for the flow around surface-mounted finite-height square prisms”, *J. Fluid. Eng. -T ASME*, **136**(8), 081206:1-10.
- Noda, H. and Nakayama, A. (2003), “Free-stream turbulence effects on the instantaneous pressure and forces on cylinders of rectangular cross section”, *Exp Fluids*, **34**, 332-344.
- Okajima, A. (1982), “Strouhal numbers of rectangular cylinders”, *J. Fluid. Mech.*, **123**, 379-398.
- Qiu, Y., Sun, Y., Wu, Y. and Tamura, Y. (2014), “Analyzing the fluctuating pressures acting on a circular cylinder using stochastic decomposition”, *J. Fluid. Struct.*, **50**, 512-527.
- Schewe, G. (2009), “Reynolds-Number-Effects in Flow around a rectangular Cylinder with Aspect Ratio 1:5”, *Proceedings of the 5th European-African Conference on Wind Engineering*, Florence, Italy.
- Schlichting, H. (1979), *Boundary Layer Theory*, McGraw-Hill, New York.
- Shimada, K. and Ishihara, T. (1999), “Prediction of aeroelastic vibration of rectangular cylinders by k-epsilon model”, *J. Aerospace Eng.*, **12**(4), 122-135.
- Shimada, K. and Ishihara, T. (2002), “Application of modified k-epsilon model to the prediction of aerodynamic characteristics of rectangular cross-sectional cylinders”, *J. Fluid. Struct.*, **16**(4), 465-485.
- Simiu, E. and Scanlan, R. (1996), *Wind Effects On Structures*, John Wiley & Sons, New York.
- Solari, G., Carassale, L. and Tubino, F. (2007), “Proper orthogonal decomposition in wind engineering - Part

- 1: A state-of-the-art and some prospects”, *Wind Struct.*, **10**(2), 153-176.
- Tamura, Y., Suganuma, S., Kikuchi, H. and Hibi, K. (1999), “Proper orthogonal decomposition of random wind pressure field”, *J. Fluid. Struct.*, **13**, 1069-1095.
- van Oudheusden, B.W., Scarano, F., van Hinsberg, N.P. and Watt, D.W. (2005), “Phase-resolved characterization of vortex shedding in the near wake of a square-section cylinder at incidence”, *Exp. Fluids*, **39** (1), 86-98.
- Wang, X. and Gu, M. (2015), “Experimental investigation of reynolds number effects on 2D rectangular prisms with various side ratios and rounded corners”, *Wind Struct.*, **21**(2), 183-202.
- Yeung, W.W.H. (2010). “On the relationships among strouhal number, pressure drag, and separation pressure for blocked bluff-body flow”, *J. Fluid. Eng. - T ASME*, **132**(2), 021201:1-10.
- Yu, D. and Kareem, A. (1998), “Parametric study of flow around rectangular prisms using LES”, *J. Wind. Eng. Ind. Aerod.*, **77-78**, 653-662.
- Zhang, Q., Liu, Y. and Wang, S. (2014), “The identification of coherent structures using proper orthogonal decomposition and dynamic mode decomposition”, *J. Fluid. Struct.*, **49**, 53-72.